Materials Today Communications 50 (2026) 114619

Contents lists available at ScienceDirect

Materials Today Communications

journal homepage: www.elsevier.com/locate/mtcomm

A X-ray view on solutal melting in Cu-Pd

Nagarjuna Remalli [a,*], Huai Zhang [a,b], Nisha Singh [a], Nuria Navarrete [a], Julien Zollinger [c], Florian Kargl [a,d]

[a] Institute for Frontier Materials on Earth and in Space, German Aerospace Center, Cologne, 51147, North-Rhine Westphalia, Germany
[b] Department of Mechanical Engineering, University of Alberta, Edmonton, AB T6G 2G8, Alberta, Canada
[c] Université de Lorraine, Institut Jean Lamour, Department of Metallurgy & Materials Science and Engineering, Allée André Guinier - ARTEM Campus, F-54000, Nancy, France
[d] Foundry Institute, RWTH Aachen University, Aachen, 52046, North-Rhine Westphalia, Germany

HIGHLIGHTS

- A reliable method was developed to derive composition from X-ray radiography, consistent with SEM-EDS measurements.
- Persistent non-equilibrium conditions were observed at the s-l interface regardless of sample thickness or melting mechanism.
- Despite non-equilibrium conditions, interface migration nearly ceased, with s-l interface velocity <1 μm/s.

GRAPHICAL ABSTRACT

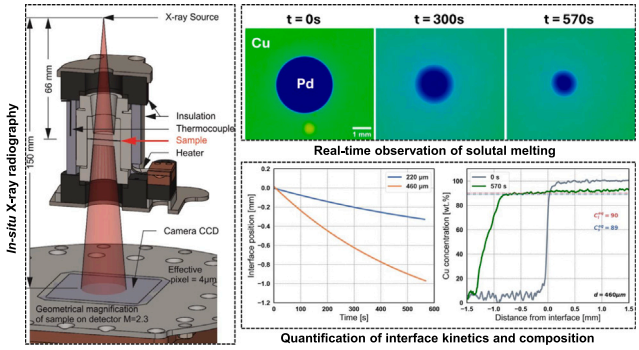

ARTICLE INFO

Keywords:
Additive manufacturing
Remelting
Melting mechanisms
Solid-liquid interface
Non-equilibrium

ABSTRACT

Solutal melting experiments on isomorphous copper-palladium (Cu-Pd) melting couples are performed to better understand the kinetics of the solid-liquid (s-l) interface. *In-situ* monitoring of the melting process with a sub-second time-resolution by X-ray radiography (XRR) is key to identifying the evolution of the concentration fields during the process. The samples used, were concentric. XRR experiments were performed using thin samples of 220 and 460 μm thickness. The samples were processed in a near-isothermal furnace by rapid heating at approximately 19.5 °C/min followed by annealing at holding temperature of 1090 °C slightly above the melting point of copper (Cu) (1085 °C) but far below the melting point of palladium (Pd) (1555 °C). Solutal melting of Pd was uniformly observed in real-time. In our study particular attention was paid to study the effect of specimen thickness on the s-l interface velocity. Pd dissolved rapidly in the thick sample of 460 μm in comparison with the thin sample of 220 μm. Furthermore, the evolution of *in-situ* concentrations was determined using transmitted X-ray intensities. Postmortem analysis performed on re-solidified CuPd alloy using SEM showed satisfactory agreement. Persistent non-equilibrium conditions existed at the s-l interface by the end of melting regardless of the melting mechanism and/or sample thickness.

* Corresponding author.
Email address: nagarjuna.remalli@dlr.de (N. Remalli).

https://doi.org/10.1016/j.mtcomm.2026.114619
Received 6 November 2025; Received in revised form 22 December 2025; Accepted 2 January 2026
Available online 7 January 2026

1. Introduction

Additive manufacturing (AM) is a promising fabrication technology to tailor three-dimensional intricate products, layer upon layer. However, the adoption of AM in critical sectors such as aerospace, is hindered due to the heterogeneity of mechanical properties and poor microstructure with deleterious defects (e.g., porosity) [1,2]. Recently, some real-time investigations have attempted to uncover the mechanisms of porosity formation during laser-matter interaction in AM [3–5]. However, these investigations have exclusively addressed the effect of thermal melting on the final microstructure. Since the AM process occurs layer upon layer, a remelting of the solidified layer (locally) would happen when it comes into contact with a fused liquid layer, driven by thermal gradient and/or solute redistribution. This process is crucial in shaping the final microstructure, thus influencing the mechanical properties. For instance, the remelting of secondary dendrite arms at the root leads to defect formation [6] and the columnar-to-equiaxed transition [7]. Additionally, AM has emerged as a promising route for fabricating bimetallic materials with tailored features and site-specific properties to satisfy the demanding industrial applications [8]. The characteristics of the interfacial region, however, are strongly influenced by the sequence of material deposition, which governs subsequent microstructural evolution and, ultimately, the resultant mechanical properties. For example, in the AM of stainless steel 316L/Inconel 718 (SS316L/IN718) bimetallic systems, deposition of IN718 onto SS316L promotes epitaxial solidification and the formation of a sharp interface. In contrast, deposition of SS316L onto IN718 results in melt pool banding, significant dilution, and the absence of epitaxial growth [9].

Melting is not simply the inverse of solidification, as emphasized by Markus Rettenmayr; although both involve solid-liquid (s-l) phase transitions [10]. They differ fundamentally in nucleation, solute concentration, and interfacial thermodynamics [10–14]. Despite its technological importance, remelting, particularly solute-driven melting has received little systematic investigation. Moreover no in-depth *in-situ* study has been conducted to examine the evolution of solute concentration together with the s-l interface kinetics. The present research aims to address this scientific gap.

Solutal melting (SM) is defined as the dissolution of a solid below its melting point when it is brought into contact with a liquid of different composition and under isothermal conditions. While the system tries to reach thermodynamic equilibrium, the asymmetry of the diffusion coefficients between the solid and the liquid phases leads to a shift between the interface velocity—governed by diffusive fluxes—and the diffusive velocity required to reach local thermodynamic equilibrium, making solutal melting an out-of-equilibrium process [15,16]. For instance, in a Cu–Ni couple (consisting of pure Cu and Ni held together) annealed isothermally at 1115 °C, thermally melted liquid Cu was in contact with solid Ni (T_m = 1455 °C). Since the compositions at the newly formed s-l interface were out of equilibrium, continuous dissolution of Ni occurred, allowing direct observation of the temporal evolution of the s–l interface [15]. However, the mechanism of solid metal dissolution in liquid remains debated. The conventional melting theory postulates that dissolution occurs through the detachment of atoms from the solid surface, followed by their diffusion into the bulk liquid [17,18]. In contrast, an alternative theory proposes that atoms from the liquid melt diffuse into the solid, forming a compositionally modified interfacial layer that melts below the solid's melting point [19]. Understanding the melting mechanism is essential for advancing technologies such as AM and welding of dissimilar metals, yet such knowledge remains scarce.

Regardless of the melting mechanism, Dutta et al. have determined the s-l interface velocity during solutal melting of the Al-Mg alloy using simple heat balance calculations [12] related to a decrease in temperature due to the consumption of latent heat [11]. Furthermore, they have claimed that the experimentally derived s-l interface velocity was in line with the simulation results [14]. Deillon et al. have examined the SM process in the Cu-Ni system in real-time at the temperatures of 1115–1145 °C using laser confocal microscopy. They observed that the dissolution rate of Ni into liquid Cu increased with increasing annealing temperature [15]. Although the progressive dissolution of Ni caused a radial composition gradient in liquid Cu, this technique was not compatible with tracking the compositional changes near the s-l interface which would affect the s-l interface kinetics. To overcome these limitations, X-ray radiography (XRR) was considered by Abdedou et al., which is a powerful technique for monitoring the s-l interface kinetics and the compositional changes simultaneously. Thin foils of Ag-Au melting couples were considered for *in-situ* SM experiments at 1000 °C. The composition analysis by XRR followed by postmortem analysis using a scanning electron microscope (SEM) revealed that non-equilibrium conditions existed at the s-l interface despite the fact that the s-l interface stagnated after 200 s during the SM process [16]. This unusual behavior of the s-l interface remains elusive. The present research is focused on better understanding the s-l interface evolution and the effect of specimen's thickness on their kinetics through *in-situ* monitoring of the melting process with a sub-second time-resolution by XRR. A particular attention was paid to study the role of melting mechanisms on the thermodynamic conditions existing at the s-l interface in the remelted zone.

2. Experimental methods

2.1. Fabrication of Cu-Pd melting couple

The well-known isomorphous Cu–Ni melting couple is convenient to fabricate via casting. However, due to the similar densities and atomic numbers of Cu and Ni, distinguishing between them using absorption-contrast XRR is challenging. As a result, this system is not ideal for XRR investigations. On the other hand, the Ag–Au melting couple is well suited for such studies, but fabricating thin samples is difficult, and both Ag and Au are costly materials for casting. Additionally, Abdedou et al. have reported buckling in thin Ag–Au samples [16], which can affect the gray values in X-radiographs and potentially mislead data interpretation. To address these limitations, the Cu-Pd melting couple is considered a promising alternative for conducting *in-situ* solutal melting experiments using XRR. Similar to the Cu-Ni and the Ag-Au systems, it is also an isomorphous system [20]. A Pd rod (99.95% purity) of 3 mm diameter and Cu shots (99.9% purity) of 1–10 mm are procured from ChemPur GmbH, Germany and Johnson Matthey GmbH, England, respectively, to fabricate Cu-Pd melting couples. Concentric samples of 11 mm diameter have been fabricated by casting Cu into a BN-coated steel-mold under an inert Argon atmosphere. The steel-mold contained a short 3 mm diameter Pd-rod at its center around which the Cu solidified. For the XRR experiments thin samples of 220 and 460 μm thickness, respectively were manufactured by slicing 1 mm discs from the as-cast Cu-Pd rod and grinding them to the desired thickness using SiC-abrasive paper.

2.2. In-situ solutal melting with X-ray radiography

An in-house built rotatable XRR facility [21,22] was used to monitor the evolution of the s-l interface and to track the radial composition changes during the melting process of the Cu-Pd melting couple. The XRR facility can be tilted 90° between the horizontal and the vertical beam direction with respect to the gravitational force. For the current research a vertical alignment of the XRR facility is considered to keep the thin samples in a near-isothermal furnace [23] aligned perpendicular to gravity so that buoyancy-driven fluid flow is suppressed. Fig. 1 shows the schematic representation of the XRR setup attached to the near-isothermal furnace in vertical alignment. The entire furnace setup was positioned in the X-ray beam to monitor the melting process with a sub-second time-resolution. Thin samples are firmly positioned in the

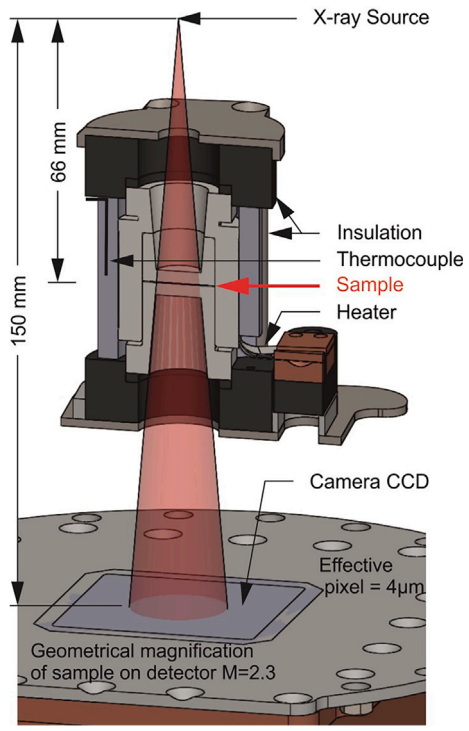

Fig. 1. XRR setup attached with near-isothermal furance in a vertical alignment [23].

center of the near-isothermal furnace made of BN to anneal them isothermally at 1090 °C for 600 s. A vacuum of 10^{-4} mbar was maintained in the cartridge prior to heating the furnace at a rapid heating rate of approximately 19.5 °C/min to reach the isothermal temperature of 1090 °C. This temperature is slightly above the melting point of Cu (1085 °C) but far below the melting point of Pd (1555 °C). Consequently, the thermally melted liquid Cu was in contact with solid Pd. Since the liquid and solid compositions at the newly formed s-l interface were out of equilibrium, the dissolution of Pd takes place. The XRR was operated at a voltage and a current of 90 kV and 90 μA, respectively, to obtain the best quality radiographs for the here presented Cu-Pd melting couple. The entire isothermal melting process, *i.e.,* the temporal evolution of the s-l interface and of radial compositional changes were monitored with an effective resolution of 4 μm [23].

2.3. Data processing method

The X-radiographs are recorded with a resolution of 3000×2840 pixels and a standard exposure rate of one frame per second. The noise in the radiographs was reduced by averaging intensities over four images using the image processing package Fiji [24]. Since each image was captured with a standard exposure rate of 1 fps, the processed images have a frame interval of 4 s. The X-radiograph shows contrast between Cu and Pd owing to a variation in their mass absorption coefficients and the densities. Typically, the dense and higher-Z solid Pd appears darker than liquid Cu. The sharp transition in gray values was used to identify the s-l interface position. The procedure of tracking the temporal evolution of the s-l interface and of determining the radial composition gradient in liquid Cu is explained in detail in the following sections. The Python programming language (Python Software Foundation, version 3.12, available at https://www.python.org/) was used for data processing using custom Python scripts written by the author (unpublished).

Tracking the s-l interface evolution

Although the original X-radiographs are acquired as 8-bit gray-scale images, they are rendered here in this article using false-color mapping to facilitate enhanced visualization of the s–l interface and the radial compositional gradient within the liquid Cu. In the color-mapped representations, regions corresponding to pure solid Pd and pure liquid Cu are shown in blue and pale green, respectively (cf. the background of Fig. 2). The Pd uptake in liquid Cu during melting leads to a darker green.

The spatial pixel intensity profiles shown in Fig. 2 as a function of distance from the original s-l interface are extracted along the red dash-dotted (3 mm in length) line positioned near the interface between solid Pd and liquid Cu in a 220 μm thin sample, at two temporal snapshots: $t = 0$ s (onset of melting) and $t = 570$ s (completion of melting). A sharp change in the pixel intensity profile is observed at the s–l interface, which is defined as the reference position (0 mm) as illustrated in Fig. 2(a). Distances extending into the liquid Cu and solid Pd phases are represented on the positive and negative scales, respectively. As melting proceeds, the dissolution of Pd into the Cu melt induces a leftward migration of the s–l interface, as illustrated in Fig. 2(b). The determined raw interface position versus time data were first smoothed using a Savitzky-Golay filter (window length = 11, polynomial order = 3) to suppress high-frequency noise while preserving the underlying trend. The smoothed data were then fitted with an exponential decay function, $y = A \cdot \exp(-k \cdot x) + C$, yielding an excellent goodness of fit ($R^2 = 0.99$), indicating that the functional form accurately represents the measured interface evolution. The fitted curve was used to represent the temporal

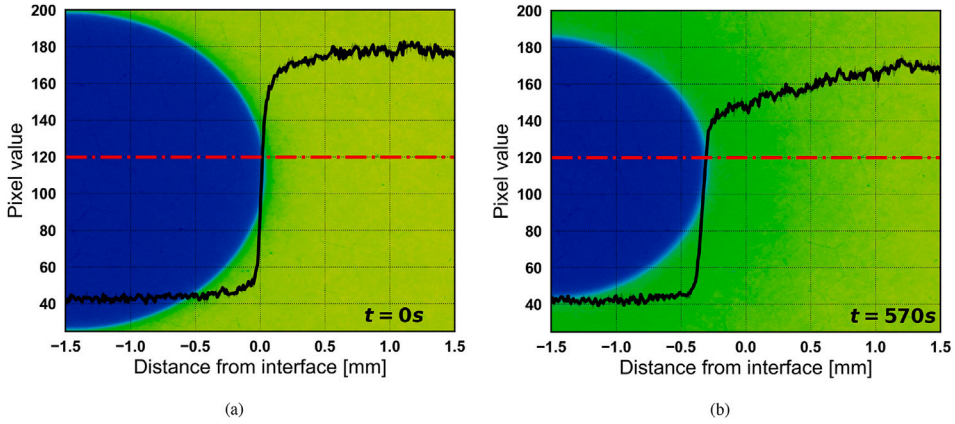

Fig. 2. The spatial pixel intensity profiles extracted along a red dash-dotted (3 mm in length) line positioned near the interface between solid Pd and liquid Cu in a 220 μm thin sample, at two temporal snapshots: (a) $t = 0$ s (onset of melting) and (b) $t = 570$ s (completion of melting).

Table 1
The pixel intensities of pure liquid Cu and solid Pd at 1090 °C.

d (μ m)	I_0	I^l_{Cu}	I^s_{Pd}
220	219.7	180.0	43.0
460	219.7	144.0	24.0

evolution of the interface position. The interface velocity was subsequently obtained by numerically differentiating the fitted curve, rather than the raw data. This approach substantially reduces numerical artifacts associated with the direct differentiation of noisy measurements and yields a smooth, physically consistent velocity profile, including velocities near the end of melting. Concurrently, the Pd diffusion into the Cu melt also leads to a radial concentration gradient within the liquid Cu adjacent to the interface. This is manifested in the form of a progressive increase in pixel intensity values in the liquid Cu region, along with a corresponding shift in color contrast, indicative of increasing Pd content in the melt (s. Fig. 2(b)).

Composition determination

Elemental concentrations were quantified from gray-level intensities using the Beer–Lambert law, which relates X-ray attenuation to material thickness d, density ρ, and mass attenuation coefficients μ_m. For monochromatic radiation, the transmitted intensity I is given by:

$$I = I_0 \cdot \exp(-\mu_m \cdot \rho \cdot d) \tag{1}$$

with I_0 being the transmitted intensity of the detector without sample. For a binary mixture of Cu-Pd in a single phase (either solid or liquid), a linear mixing rule applies:

$$\mu_m \cdot \rho = x_{Cu} \cdot \mu_{m,Cu} \cdot \rho_{Cu} + x_{Pd} \cdot \mu_{m,Pd} \cdot \rho_{Pd} \tag{2}$$

where x_{Cu}, x_{Pd} are the weight fractions of the elements Cu and Pd, respectively. Rearranging Eq. (1) the liquid Cu composition is obtained as:

$$x^l_{Cu} = \frac{\left[\left(\frac{1}{d}\right) \cdot \ln\left(\frac{I_0}{I}\right)\right] - \left(\mu^l_{m,Pd} \cdot \rho^l_{Pd}\right)}{\left(\mu^l_{m,Cu} \cdot \rho^l_{Cu}\right) - \left(\mu^l_{m,Pd} \cdot \rho^l_{Pd}\right)}. \tag{3}$$

The sample thickness d was held constant throughout the melting process by applying a controlled pressure via a piston within a near-isothermal furnace, thereby eliminating thickness variation as a contributing factor to changes in detector intensity profiles. The incident X-ray intensity, I_0, was determined from images acquired in the absence of the sample. For a poly-chromatic X-ray source, the effective mass absorption coefficients for Cu and Pd in relevant solid/liquid phases were calibrated empirically using the measured gray-scale intensities of pure reference materials. Specifically, the absorption coefficients for liquid Cu ($\mu^l_{m,Cu}$) and solid Pd ($\mu^s_{m,Pd}$) at 1090 °C were obtained from Beer–Lambert law (Eq. 1):

$$\mu^l_{m,Cu} = \frac{\ln\left(\frac{I_0}{I^l_{Cu}}\right)}{d \cdot \rho^l_{Cu}}$$
$$\mu^s_{m,Pd} = \frac{\ln\left(\frac{I_0}{I^s_{Pd}}\right)}{d \cdot \rho^s_{Pd}}. \tag{4}$$

where I^l_{Cu} and I^s_{Pd} correspond to the pixel intensities of pure liquid Cu and solid Pd, respectively, measured immediately prior to melting (s. Table 1).

The absorption coefficient for pure Pd in the liquid phase ($\mu^l_{m,Pd}$), required for subsequent composition analysis via Eq. (3), was not directly accessible. Following the approach reported by Abedou et al. [16], $\mu^l_{m,Pd}$ was approximated based on the inverse ratio of densities between the phases:

$$\mu^l_{m,Pd} \approx \mu^s_{m,Pd} \cdot \frac{\rho^s_{Pd}}{\rho^l_{Pd}}. \tag{5}$$

Table 2
The mass absorption coefficients and densities of Cu and Pd at 1090 °C.

d (μ m)	Material	μ^s_m (cm^2 g^{-1})	μ^l_m (cm^2 g^{-1})	ρ^s (g cm^{-3})	ρ^l (g cm^{-3})
220	Cu	1.07	1.17	8.49	7.83
	Pd	6.44	6.75	11.55	11.02
460	Cu	1.09	1.18	8.49	7.83
	Pd	4.21	4.41	11.55	11.02

The phase-specific densities ρ^l_{Cu} and ρ^s_{Pd} at 1090 °C were obtained from the literature [25–27] are tabulated (s. Table 2). While this represents a reasonable first-order approximation, effective attenuation in a poly-chromatic X-ray beam may deviate from linear density scaling. To assess the sensitivity of the reconstructed composition profiles to this assumption, the liquid Pd attenuation coefficient was varied by ±10% relative to the density-scaled reference value, and the full reconstruction procedure was repeated. The analysis shows that variations in the assumed liquid Pd attenuation coefficient mainly affect the absolute attenuation within the fully solid Pd region, while the position of the s-l interface, the solute concentration gradients in the liquid Cu region, and the overall profile morphology remain essentially unchanged.

Additionally, postmortem analysis of the re-solidified alloys was performed using field-emission SEM. The re-solidified Cu-Pd samples were polished with BUEHLER MasterPrep polishing solution with an average grain size of 0.05 μm. Data were acquired using a ZEISS Gemini SEM operated at 7 kV and 2 nA in back-scattered electron (BSE) imaging mode. Energy Dispersive Spectroscopy (EDS) measurements were performed using an Oxford Instruments detector, and AZtec software was used for data acquisition and post-processing.

3. Experimental results

3.1. Preliminary SEM studies

The process of Cu-Pd melting couples fabricated here closely resembles the solutal melting process, with liquid Cu contacting a solid Pd rod (refer Section 2.1). Based on Deillon's study on the Cu-Ni melting couple, the presence of a pre-existing inter diffusive layer influences s-l interface kinetics during the melting process [15]. Therefore, inter diffusion at the Cu-Pd interface during casting must be assessed. Prior to SM experiments, the as-cast Cu-Pd rod was analyzed using SEM-EDS for compositional analysis across the Cu-Pd interface, sampling from both the bottom and top sections. Fig. 3 presents BSE micrographs of the as-cast Cu-Pd rod from the bottom and top sections. The bottom section exhibits a sharp interface with no detectable inter-diffusion (s. Fig. 3(a)), whereas the top section shows a 2 μm diffusive layer (s. Fig. 3(b)), attributed to slower heat extraction during solidification. To eliminate any influence of the pre-existing diffusive layer on the s-l interface kinetics, solutal melting experiments were conducted exclusively on Cu-Pd melting couples sliced from the bottom section of the as-cast rod.

3.2. Solutal melting of Cu-Pd couple

Solutal melting experiments were performed on two samples of 220 and 460 μm thickness. Each was annealed in a near-isothermal furnace at 1090 °C, slightly above the melting point of Cu (1085 °C) and well below that of Pd (1555 °C), resulting in liquid Cu in contact with solid Pd. Fig. 4 illustrates Pd dissolution into liquid Cu during the melting of 220 μm thin sample and 460 μm thick sample (video files are provided as Supplementary material). Pd dissolution occurs uniformly across the

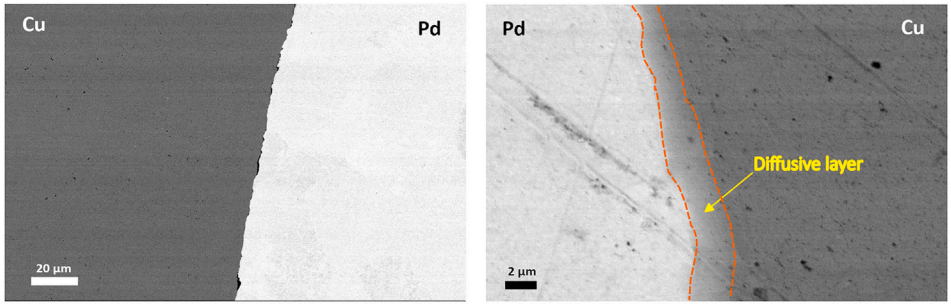

Fig. 3. BSE micrographs of as-cast Cu-Pd interface, sampling from both the (a) bottom and (b) top sections.

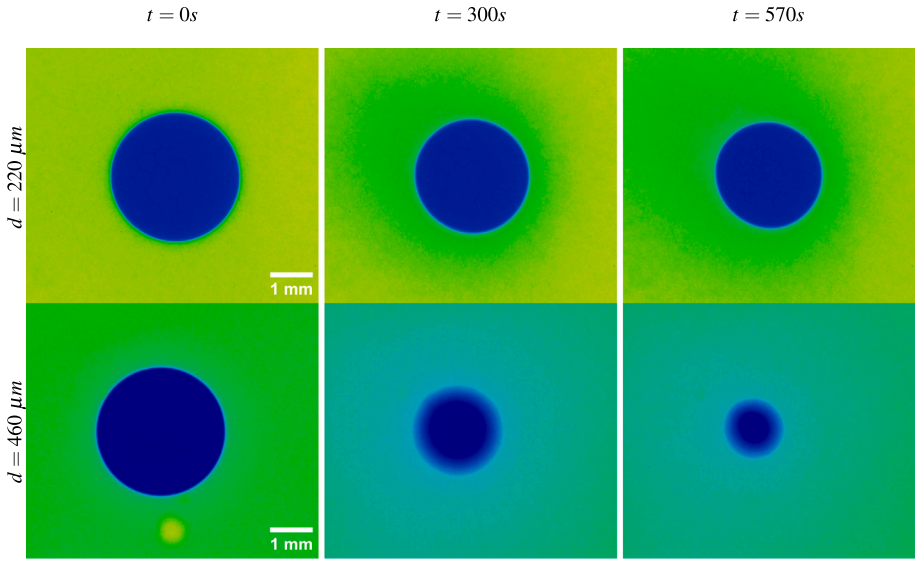

Fig. 4. False-color representations of X-radiographs illustrate Pd dissolution into liquid Cu during melting at 1090 °C; Top row: 220 μm thin sample; Bottom row: 460 μm thick sample.

interface, but proceeds faster in the thicker 460 μm sample (s. Fig. 4 bottom row) than in the thinner 220 μm sample (s. Fig. 4 top row). Simultaneously, the evolution of solute gradients within the liquid Cu is evident from the progressive color changes in the maps.

3.3. S-l interface kinetics

As Pd dissolves into the liquid Cu during melting, the s-l interface migrates leftward (s. Fig. 2), indicating that, from the perspective of solid Pd, the interface progressively recedes with time. The temporal evolution of s–l kinetics and solute gradients in liquid Cu were quantified from the processed data (refer to Section 2.3). Fig. 5(a) presents the interface position as function of time. The negative scale indicates a progressive recession of the s-l interface. In the thin sample, the interface receded by 330 μm, compared to 970 μm for the thick sample. The interface velocity is obtained by differentiating the interface position with respect to time. In both cases, dissolution rates decreased with time; however, the initial rate was notably lower in the thin sample (s. Fig. 5(b)).

3.4. Composition gradient in liquid Cu

The solute gradient in liquid Cu was determined from the XRR data as described in the Section 2.3. Fig. 6 shows the concentration profiles in the vicinity of the s-l interface at the beginning ($t = 0$ s) and at the end ($t = 570$ s) of the melting process. The equilibrium liquidus and solidus compositions of the Cu-Pd alloy at 1090 °C are 90 and 89 wt.% of Cu, shown as red and blue dash-dotted lines, respectively. At first glance, the composition profile at $t = 570$ s indicates that the interface receded by 330 μm (s. Fig. 6(a)), compared to 970 μm for the thick sample (s. Fig. 6(b)). Besides, the composition profiles at the end of melting indicate that liquid Cu in the 220 μm thin sample does not reach equilibrium, whereas in the 460 μm thick sample, equilibrium appears to be attained away from the s–l interface. Subsequently, postmortem analysis of the re-solidified Cu-Pd alloys were conducted using SEM to examine the Cu-Pd interface and the radial solute gradients of Cu. In principle, the width of the s–l interface is only a few atomic layers, which lies beyond the resolution limit of SEM. Therefore, in the present study, a transition zone between solid Pd and liquid Cu was analyzed using SEM. Fig. 7 presents the BSE micrographs of the re-solidified samples. For improved clarity, the inherently gray-scale BSE images are shown with false-color mapping to highlight the s–l transition zone. The regions corresponding to pure Pd and to Cu alloyed with Pd appear in uniform colors, whereas the transition zone displays a gradual change in color contrast (outlined by dashed lines in Fig. 7), which is interpreted as representing the s–l transition zone width in the re-solidified alloys. The postmortem analysis indicates an s–l transition zone width of 20–25 μm and 28–30 μm in the thin and thick specimens, respectively.

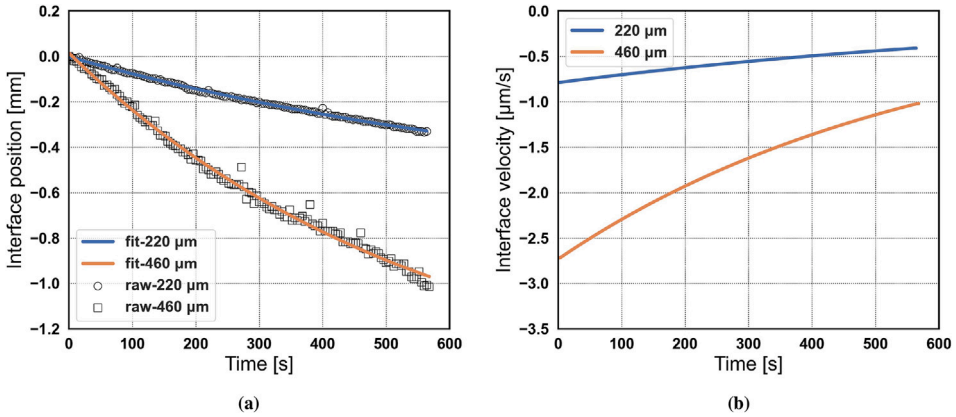

Fig. 5. The temporal evolution of s-l interface (a) position, (b) velocity during melting process at 1090 °C.

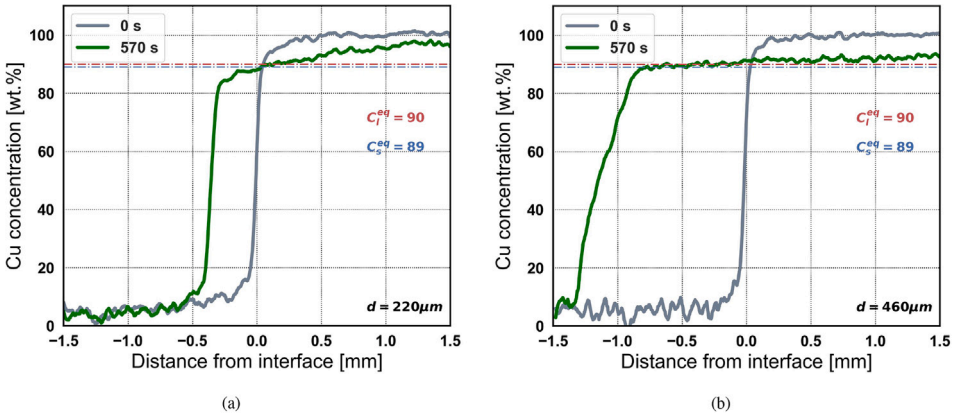

Fig. 6. Concentration profiles in (a) 220 μm thin sample, (b) 460 μm thick sample, in the vicinity of s-l interface at the beginning (t = 0 s) and at the end (t = 570 s) of melting process. The red and blue dash-dotted lines represent the equilibrium liquidus and solidus compositions, respectively.

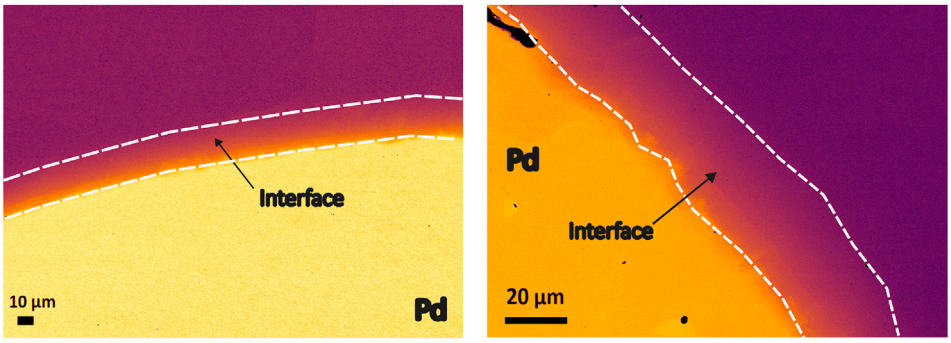

Fig. 7. BSE micrographs of re-solidified Cu-Pd alloy depicting the transition in between pure Pd and Cu alloyed with Pd (a) 220 μm thin sample and (b) 460 μm thick sample.

4. Discussion

In-situ solutal melting of isomorphous Cu-Pd couples showed uniform Pd dissolution into liquid Cu. Two specimen thicknesses, 220 and 460 μm, were used to investigate the influence of sample thickness on s–l interface evolution and melt depth, where the melt depth corresponds to the recession distance of the s-l interface. Thin specimens were held perpendicular to gravity in a near-isothermal furnace to minimize buoyancy-driven convection. Despite this, the 460 μm specimen exhibited markedly faster dissolution than the 220 μm specimen (s. Fig. 4), with s–l interface recession distances of 970 and 330 μm, respectively. The larger melt depth in the 460 μm specimen places it firmly in a regime where buoyancy-driven flow is more likely to arise. Consequently, the rapid dissolution of Pd in the 460 μm specimen was attributed to buoyancy convection leading to additional transport of solute-depleted liquid to the interface, whereas the smaller melt depth in the 220 μm specimen remains predominantly diffusion-controlled as illustrated in Fig. 8. Although no direct evidence of convection, such as grayscale fluctuations or asymmetries, was observed in the XRR measurements, indirect

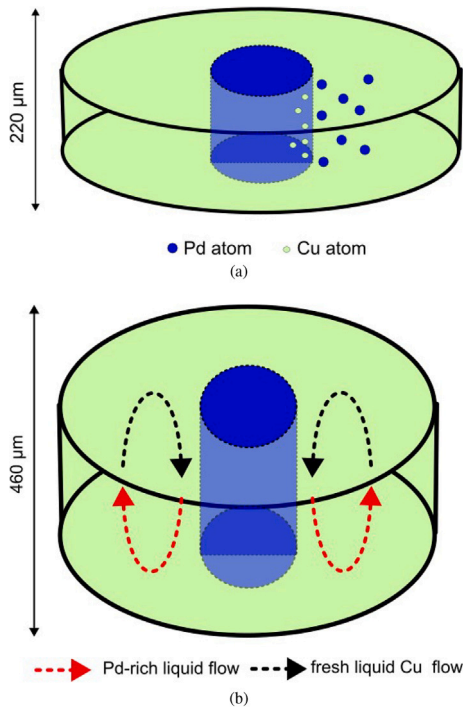

Fig. 8. Schematic representation of (a) diffusion-controlled melting in 220 μm thin sample, (b) convection-dominated melting in 460 μm thick sample.

signatures support its presence. For example, the concentration profiles of Cu melt at the end of melting (s. Fig. 6).

Pd dissolution generated a radial solute gradient in Cu melt, evident from decreasing pixel intensities near the s–l interface over time (s. Fig. 4). The concentration profiles, derived from XRR as described in Section 2.3, are shown in Fig. 6 for the initial state (t = 0 s) and at the end of melting (t = 570 s). The composition profiles at the end of melting indicate that liquid Cu in the 220 μm thin sample still varies as a sharper gradient over 1 mm from the s-l interface, whereas in the 460 μm thick sample, the composition profile is a flattened, plateau-like concentration profile as shown in Fig. 6. This difference is consistent with enhanced convective mixing in the thicker sample and reinforces the conclusion that convection plays a significant role in the observed differences in melt depth between the two sample thicknesses. This observation strongly endorses the previous statement that in the thick sample the Pd transport is enhanced by buoyancy-driven convection.

To quantify the transition between diffusion- and convection-dominated solute transport, the solutal Rayleigh number (Ra_s) was estimated using thermophysical data for silver-copper (Ag–Cu) as a proxy system, due to the absence of Cu-Pd liquid-state properties in the literature. Ag was selected because it is adjacent to Pd in the periodic table and exhibits similar solution behavior in liquid Cu. The current XRR setup is not suitable for determining the concentration gradient ΔC in the gravity direction. Hence, ΔC and s-l interfacial compositions are assumed to be 0.5% and 50–50 wt.%, respectively. The parameters used for the calculation are summarized in Table 3. The solutal Rayleigh number is defined as

$$Ra_s = \frac{g \cdot \beta_s \cdot \Delta C \cdot H^3}{\nu \cdot D} \tag{6}$$

where g is gravitational acceleration, $\beta_s = \left(\frac{-1}{\rho}\right) \cdot \left(\frac{\partial \rho}{\partial C}\right)$ is the solutal expansion coefficient, ΔC is the concentration difference, H is the specimen height, $\nu = \frac{\eta}{\rho}$ is the kinematic viscosity, and D is the solute diffusivity [28]. The solutal expansion coefficient is approximated

Table 3
Parameters used for estimating the solutal Rayleigh number for Cu-Pd using Cu-Ag thermophysical data as a proxy.

Parameter	Value	Source
g	9.81 m s^{-2}	
H	220 – 460 μm	
ρ_{Cu-Ag}	9155 kg m^3	Estimated
β_s	0.338	Estimated
η	3.2 mPa s	[30]
$\nu = \eta/\rho$	3.50 m^{2}s^{-1}	Estimated
D	3.03 × 10^{-9} m^{2}s^{-1}	[31]

from volumetric expansion, *i.e.,* $\beta_s = \left(\frac{1}{\rho \cdot V^2}\right) \cdot \left(\frac{\partial V}{\partial C}\right)$ at the interfacial alloy composition of 50–50 wt.%. Using the parameters in Table 3, the solutal Rayleigh numbers Ra_s for the 220 μm and 460 μm samples are 167 and 1525, respectively. Typical critical Rayleigh numbers for buoyancy-driven solutal convection in simple layer geometries are on the order of 10^3 [29]. Thus, the 220 μm specimen lies safely within the diffusion-dominated regime, whereas the 460 μm specimen approaches the convection onset threshold. This is consistent with the experimentally observed transport behavior: the thicker 460 μm specimen displays significantly flatter concentration profiles compared with the sharp, diffusion-controlled gradient in the 220 μm thin sample.

Fig. 9 compares the composition profiles obtained from XRR data at the end of the experiment (*i.e.,* at 570 s) with postmortem SEM-EDS analysis on re-solidified Cu-Pd alloy. It shows close agreement between XRR-derived radial concentration gradients and EDS measurements, confirming negligible beam-hardening effects in polychromatic XRR under these experimental conditions. In addition, quantitative SEM-EDS line scans were acquired in the vicinity of the s-l interface on specimens with thicknesses of 220 μm and 460 μm (s. Fig. 10). The normalized profiles show the variation in elemental composition across the s-l interface, with measurement uncertainty, confirming the previously observed compositional trends. The relatively higher noise in the Cu-Pd alloy region compared with the pure Pd domain is attributed to micro-segregation during resolidification. This shows that the method presented to determine composition from the grayscale X-radiographs is consistent for the Cu-Pd system. Postmortem analysis revealed transition zone widths of 20–25 μm in the 220 μm thin specimen and 28–30 μm in the 460 μm thick specimen (s. Fig. 7), which is indicated by chocolate-colored vertical dashed lines in Fig. 9. Using composition data obtained from XRR and SEM, the s-l interface compositions at t = 570 s were ≈50–60 wt.% Cu for the thin sample and ≈70–75 wt.% Cu for the thick sample, indicating that non-equilibrium conditions persist at the s-l interface regardless of specimen thickness and underlying melting mechanism. These findings are consistent with prior observations in solutal melting of isomorphous Cu-Ni [15] and Ag–Au couples [16]. To contextualize the observed non-equilibrium behavior at the s-l interface, an approximate diffusion timescale analysis was performed. Since direct measurements of the diffusion coefficient of Pd in liquid Cu at 1090 °C are not available, we used the diffusivity of Ag in liquid Cu as a proxy system to estimate the characteristic diffusion length using $x = \sqrt{Dt}$. The diffusion coefficient of Ag in liquid Cu at 1090 °C is $D = 3.03 \cdot 10^{-9}$ m^2/s [31]. The resulting diffusion distance over t = 570 s is approximately $x \approx 1314$ μm. Surprisingly, this length is much larger than the measured melt depth (*i.e.,* the recession distances of s-l interface). Although diffusion coefficient suggests relatively rapid solute transport in liquid Cu, the *in-situ* XRR and EDS measurements still reveal non-equilibrium solute gradients at the s-l interface. This indicates that additional kinetic limitations beyond simple diffusion may be active. Despite the non-equilibrium state, interface migration rates diminished to <1 μm/s by the end of melting (s. Fig. 5(b)). These results pave the way for further investigations into the precise quantification of interface kinetics and concentration evolution by probing the s-l interface at atomic resolution

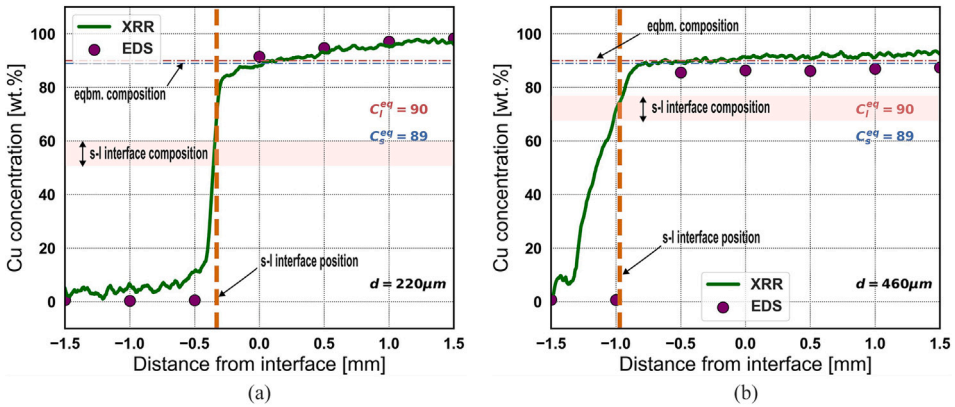

Fig. 9. Comparison of concentration profiles measured using SEM-EDS and XRR in (a) 220 μm thin sample, (b) 460 μm thick sample, in the vicinity of s-l interface at the end of melting (t = 570 s); the vertical dashed line in chocolate color represents the interface position.

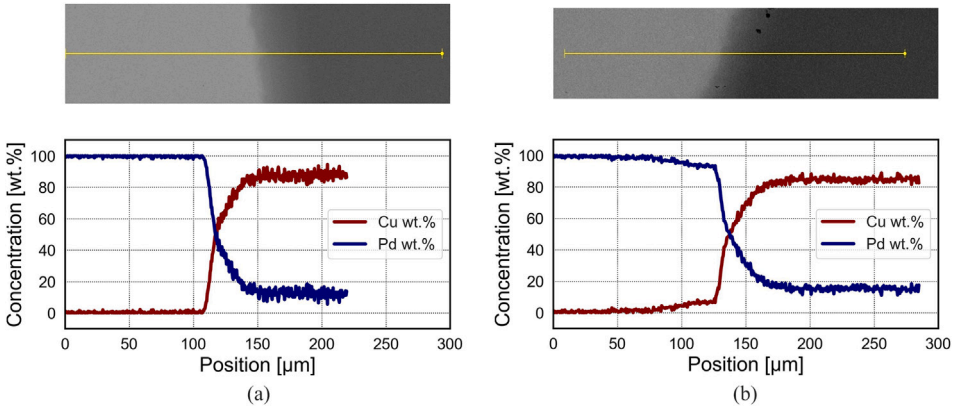

Fig. 10. Representative EDS line scans in the vicinity of s-l interface of (a) 220 μm thin sample, (b) 460 μm thick sample.

in real-time. This will provide insight into the out-of-equilibrium aspects of solutal melting.

5. Summary

Pd dissolved uniformly in liquid Cu. However, the sample thickness plays a key role on the dissolution rate. The s-l interface was receded by 330 μm in the thin sample, which is attributed to the diffusion-controlled dissolution of Pd. In the thick sample, the s-l interface was receded by 970 μm. The rapid dissolution of Pd was attributed to additional convective transport contributions besides Pd inter-diffusion. XRR-derived radial composition gradients and EDS measurements, confirm negligible beam-hardening effects in poly-chromatic XRR for these experimental conditions. The composition profiles indicate that persistent non-equilibrium conditions existed at the s-l interface regardless of sample thickness and/or the underlying melting mechanism. Flattened concentration profiles in the thick sample versus steep gradient profiles in the thin sample, along with estimated solutal Rayleigh numbers, indicate the transition from diffusion-dominated to convection-influenced transport. Despite the non-equilibrium state, interface migration rates diminished to <1 μm/s by the end of melting, highlighting kinetic limitations with implications for additive manufacturing, welding, and solidification processes, which need to be further studied.

CRediT authorship contribution statement

Nagarjuna Remalli: Writing – original draft, Methodology, Investigation, Conceptualization. **Huai Zhang:** Investigation. **Nisha Singh:** Investigation. **Nuria Navarrete:** Investigation. **Julien Zollinger:** Writing – review & editing. **Florian Kargl:** Writing – review & editing, Supervision, Project administration.

Declaration of competing interest

The authors declare that they have no known competing financial interests or personal relationships that could have appeared to influence the work reported in this paper.

Acknowledgments

The author acknowledges support from the DLR–DAAD program through a postdoctoral fellowship. Constructive discussions on experimental design with Christoph Dreißigacker and Golo Zimmermann are gratefully recognized. The author would like to thank his colleague, Marimel Mayer, for her careful proofreading and valuable feedback on the manuscript.

Appendix A. Supplementary data

Supplementary data for this article can be found online at doi:10.1016/j.mtcomm.2026.114619.

Data availability

Data will be made available on request.

References

[1] N.T. Aboulkhair, N.M. Everitt, I. Ashcroft, C. Tuck, Reducing porosity in AlSi10Mg parts processed by selective laser melting, Addit. Manuf. 1 (2014) 77–86.

[2] C. Qiu, S. Yue, N.J. Adkins, M. Ward, H. Hassanin, P.D. Lee, P.J. Withers, M.M. Attallah, Influence of processing conditions on strut structure and compressive properties of cellular lattice structures fabricated by selective laser melting, Mater. Sci. Eng. A 628 (2015) 188–197.
[3] C. Zhao, K. Fezzaa, R.W. Cunningham, H. Wen, F. De Carlo, L. Chen, A.D. Rollett, T. Sun, Real-time monitoring of laser powder bed fusion process using high-speed X-ray imaging and diffraction, Sci. Rep. 7 (1) (2017) 3602.
[4] C.L.A. Leung, S. Marussi, M. Towrie, J. del Val Garcia, R.C. Atwood, A.J. Bodey, J.R. Jones, P.J. Withers, P.D. Lee, Laser-matter interactions in additive manufacturing of stainless steel SS316L AND 13-93 bioactive glass revealed by in situ X-ray imaging, Addit. Manuf. 24 (2018) 647–657.
[5] C.L.A. Leung, S. Marussi, R.C. Atwood, M. Towrie, P.J. Withers, P.D. Lee, In situ X-ray imaging of defect and molten pool dynamics in laser additive manufacturing, Nat. Commun. 9 (1) (2018) 1355.
[6] M. Schneider, J. Gu, C. Beckermann, W. Boettinger, U. Kattner, Modeling of micro-and macrosegregation and freckle formation in single-crystal nickel-base superalloy directional solidification, Metall. Mater. Trans. A 28 (1997) 1517–1531.
[7] S. Flood, J. Hunt, Metals Handbook—castings, vol. 15, ASM INTERNATIONAL, Metals Park, OH, 1998, pp. 130–136.
[8] A. Bandyopadhyay, Y. Zhang, B. Onuike, Additive manufacturing of bimetallic structures, Virt. Phys. Prototyp. 17 (2) (2022) 256–294.
[9] S. Goswami, V. Minnikanti, S. Mishra, S. Karagadde, Interfacial phenomena in additively manufactured stainless steel 316l/inconel 718 multi-material structures, Trans. Indian Inst. Met. 77 (10) (2024) 3013–3018.
[10] M. Rettenmayr, Solidification and melting processes—one of the fundamental asymmetries in nature, Trans. Indian Inst. Met. 62 (4) (2009) 265–268.
[11] M. Rettenmayr, O. Warkentin, H.E. Exner, Deviations from equilibrium at remelting solid/liquid interfaces, Int. J. Mater. Res. 88 (8) (2021) 617–619.
[12] B. Dutta, M. Rettenmayr, An experimental investigation on the kinetics of solute driven remelting, Metall. Mater. Trans. A 31 (2000) 2713–2720.
[13] M. Rettenmayr, Melting and remelting phenomena, Int. Mater. Rev. 54 (1) (2009) 1–17.
[14] M. Rettenmayr, O. Warkentin, M. Rappaz, H. Exner, Simulation of solutal remelting, Acta Mater. 49 (13) (2001) 2499–2510.
[15] L. Deillon, J. Zollinger, D. Daloz, M. Založnik, H. Combeau, In-situ observations of solutal melting using laser scanning confocal microscopy: the Cu/Ni model system, Mater. Charact. 97 (2014) 125–131.
[16] N. Abdedou, Non-equilibrium conditions at solid/liquid interfaces, Ph.D. thesis, 2023, Université de Lorraine.
[17] W. Kaysser, G. Petzow, Present state of liquid phase sintering, Powder Metall. 28 (3) (1985) 145–150.
[18] V.I. Nikitin, Physicochemical phenomena in the action of liquid metals on solid, Atomizdat, Moscow (1967) (1967).
[19] A.P. Savitskii, Diffusion interaction between two metals, one of which is in liquid state, in: Materials Science Forum, vol. 575, Trans Tech Publ, 2008, pp. 1477–1482.
[20] P. Subramanian, D. Laughlin, Cu-Pd (copper-palladium, J. Phase Equilib. 12 (2) (1991) 231–243.
[21] F. Kargl, J. Drescher, C. Dreißigacker, M. Balter, M. Becker, M. Wegener, E. Sondermann, Xrise-M: X-radiography facility for solidification and diffusion studies of alloys aboard sounding rockets, Rev. Sci. Instrum. 91 (1) (2020).
[22] S. Klein, D. Braeuer, M. Becker, A. Knipstein, S. Meckel, E. Sondermann, F. Kargl, X-rise-A multifunctional X-ray radiography device for parabolic flights and laboratory use, Int. J. Microgravity Sci. Appl. 33 (4) (2016) 330405.
[23] M. Becker, C. Dreißigacker, S. Klein, F. Kargl, Near-isothermal furnace for in situ and real time X-ray radiography solidification experiments, Rev. Sci. Instrum. 86 (6) (2015).
[24] J. Schindelin, I. Arganda-Carreras, E. Frise, V. Kaynig, M. Longair, T. Pietzsch, S. Preibisch, C. Rueden, S. Saalfeld, B. Schmid, et al., Fiji: an open-source platform for biological-image analysis, Nat. Methods 9 (7) (2012) 676–682.
[25] M. Watanabe, M. Adachi, H. Fukuyama, Densities of AU-X (X= Cu, Ni and Pd) binary melts and thermodynamic correlations, J. Mol. Liq. 348 (2022) 118050.
[26] D.R. Lide, Handbook of Chemistry and Physics, 2006.
[27] P.-F. Paradis, T. Ishikawa, Y. Saita, S. Yoda, Containerless property measurements of liquid palladium, Int. J. Thermophys. 25 (6) (2004) 1905–1912.
[28] J.W. Lee, J.M. Hyun, Double-diffusive convection in a rectangle with opposing horizontal temperature and concentration gradients, Int. J. Heat Mass Transf. 33 (8) (1990) 1619–1632.
[29] S. Hirata, B. Goyeau, D. Gobin, Stability of thermosolutal natural convection in superposed fluid and porous layers, Transp. Porous Media 78 (3) (2009) 525–536.
[30] D. Živković, D. Manasijević, An optimal method to calculate the viscosity of simple liquid ternary alloys from the measured binary data, Calphad 29 (4) (2005) 312–316.
[31] A. Bruson, M. Gerl, Diffusion coefficients of Sb 124, Sn 113, Ag 1 1 0 M, and Au 195 in liquid copper, Phys. Rev. B 19 (12) (1979) 6123.